

Wavelength independent normal incident quantum cascade detectors

ARVIND P. RAVIKUMAR,^{1,2,*} DEBORAH SIVCO,¹ AND CLAIRE F. GMACHL¹

¹Department of Electrical Engineering, Princeton University, Princeton, NJ 08544, USA

²Currently with the Department of Energy Resources Engineering, Stanford University, Stanford, CA 94305, USA

*arvindr@stanford.edu

Abstract: We demonstrate a novel technique for normal-incident absorption in intersubband infrared detectors by taking advantage of light scattering from the side-walls of a wet-etched mesa. We fabricate ‘spiral’ and ‘hairpin’ shaped quantum cascade detector at a peak wavelength of 6.6 μm , and compare their performance with a standard rectangular mesa. We achieve a peak responsivity of 6 mA/W for the spiral and 12 mA/W for the hairpin detectors at normal incidence, comparable to the 8.8 mA/W obtained for the mesa at 45 degree incidence. We obtain a background limited detectivity of about $3 \times 10^{10} \text{ cm}\sqrt{\text{Hz}}/\text{W}$ for the spiral and hairpin detectors at 80 K, compared to $3 \times 10^8 \text{ cm}\sqrt{\text{Hz}}/\text{W}$ for the standard mesa. This method to achieve normal incidence absorption is wavelength independent, and does not involve complicated fabrication procedures, paving the way for widespread use of intersubband detectors in sensor applications.

© 2016 Optical Society of America

OCIS codes: (040.3060) Infrared; (040.5570) Quantum detectors; (230.5160) Photodetectors;

References and links

1. H. Schneider, and H. C. Liu, *Quantum Well Infrared Photodetectors* (Springer, 2007).
2. A. Harrer, B. Schwarz, S. Schuler, P. Reininger, A. Wirthmüller, H. Detz, D. MacFarland, T. Zederbauer, A. M. Andrews, M. Rothermund, H. Oppermann, W. Schrenk, and G. Strasser, “4.3 μm quantum cascade detector in pixel configuration,” *Opt. Express* **24**(15), 17041–17049 (2016).
3. A. P. Ravikumar, J. De Jesus, M. C. Tamargo, and C. F. Gmachl, “High performance, room temperature, broadband II-VI quantum cascade detector,” *Appl. Phys. Lett.* **107**(14), 141105 (2015).
4. A. P. Ravikumar, T. A. Garcia, J. De Jesus, M. C. Tamargo, and C. F. Gmachl, “High detectivity short wavelength II-VI quantum cascade detector,” *Appl. Phys. Lett.* **105**(6), 061113 (2014).
5. P. Reininger, B. Schwarz, H. Detz, D. MacFarland, T. Zederbauer, A. M. Andrews, W. Schrenk, O. Baumgartner, H. Kosina, and G. Strasser, “Diagonal transition quantum cascade detector,” *Appl. Phys. Lett.* **105**, 091108 (2014).
6. M. Z. Tidrow, K. K. Choi, A. J. DeAnni, W. H. Chang, and S. P. Svensson, “Grating coupled multicolor quantum well infrared photodetector,” *Appl. Phys. Lett.* **67**(13), 1800–1802 (1995).
7. Y. S. Larry, and S. S. Li, “A metal grating coupled bound-to-miniband transition GaAs multiquantum well/superlattice infrared detector,” *Appl. Phys. Lett.* **59**(11), 1332–1334 (1991).
8. P. Bois, E. Costard, X. Marcadet, and E. Herniou, “Development of quantum well infrared photodetectors in France,” *Infrared Phys. Technol.* **42**(3), 291–300 (2001).
9. T. R. Schimert, S. L. Barnes, A. J. Brouns, F. C. Case, P. Mitra, and L. T. Claiborne, “Enhanced quantum well infrared photodetector with novel multiple quantum well grating structure,” *Appl. Phys. Lett.* **68**(20), 2846–2848 (1996).
10. J. Y. Andersson, and L. Lundqvist, “Grating-coupled quantum-well infrared detectors: theory and performance,” *J. Appl. Phys.* **71**(7), 3600–3610 (1992).
11. E. Dupont, “Optimization of lamellar gratings for quantum-well infrared photodetectors,” *J. Appl. Phys.* **88**(5), 2687–2692 (2000).
12. L. Li, D. Xiong, J. Wen, N. Li, and Z. Zhu, “A surface plasmonic coupled mid-long-infrared two-color quantum cascade detector,” *Infrared Phys. Technol.* **79**, 45–49 (2016).
13. A. Pesach, S. Sakr, E. Giraud, O. Sorias, L. Gal, M. Tchernycheva, M. Orenstein, N. Grandjean, F. H. Julien, and G. Bahir, “First demonstration of plasmonic GaN quantum cascade detectors with enhanced efficiency at normal incidence,” *Opt. Express* **22**(17), 21069 (2014).
14. A. Harrer, B. Schwarz, R. Gansch, P. Reininger, H. Detz, T. Zederbauer, A. M. Andrews, W. Schrenk, and G. Strasser, “Plasmonic lens enhanced mid-infrared quantum cascade detector,” *Appl. Phys. Lett.* **105**, 171112 (2014).
15. W. Wu, A. Bonakdar, and H. Mohseni, “Plasmonic enhanced quantum well infrared photodetector with high detectivity,” *Appl. Phys. Lett.* **96**(16), 161107 (2010).

16. S. Zhai, J. Liu, F. Liu, and Z. Wang, "A normal incident quantum cascade detector enhanced by surface plasmons," *Appl. Phys. Lett.* **100**(18), 181104 (2012).
17. S. D. Gunapala, B. F. Levine, D. Ritter, R. Hamm, and M. B. Panish, "InGaAs/InP hole intersubband normal incidence quantum well infrared photodetector," *J. Appl. Phys.* **71**(5), 2458–2460 (1992).
18. B. F. Levine, S. D. Gunapala, J. M. Kuo, S. S. Pei, and S. Hui, "Normal incidence hole intersubband absorption long wavelength GaAs/AlxGa1-xAs quantum well infrared photodetectors," *Appl. Phys. Lett.* **59**(15), 1864–1866 (1991).
19. S. Kalchmair, H. Detz, G. D. Cole, A. M. Andrews, P. Klang, M. Nobile, R. Gansch, C. Ostermaier, W. Schrenk, and G. Strasser, "Photonic crystal slab quantum well infrared photodetector," *Appl. Phys. Lett.* **98**(1), 011105 (2011).
20. X. Wang, S. Zhai, N. Zhuo, J. Liu, F. Liu, S. Liu, and Z. Wang, "Quantum dot quantum cascade infrared photodetector," *Appl. Phys. Lett.* **104**, 171108 (2014).
21. C. J. Chen, K. K. Choi, M. Z. Tidrow, and D. C. Tsui, "Corrugated quantum well infrared photodetectors for normal incident light coupling," *Appl. Phys. Lett.* **68**(11), 1446–1448 (1996).
22. K. K. Choi, D. P. Forrai, D. W. Endres, and J. Sun, "Corrugated quantum-well infrared photodetector focal plane arrays," *IEEE J. Quantum Electron.* **45**(10), 1255–1264 (2009).
23. C. J. Chen, K. K. Choi, L. Rokhinson, W. H. Chang, and D. C. Tsui, "A characterization technique for quantum well infrared photodetectors," *Appl. Phys. Lett.* **75**(20), 3210–3212 (1999).
24. C. Sirtori, F. Capasso, J. Faist, and S. Scandolo, "Nonparabolicity and a sum rule associated with bound-to-bound and bound-to-continuum intersubband transitions in quantum wells," *Phys. Rev. B* **50**(12), 8663–8674 (1994).

1. Introduction

It is widely known that polarization selection rules for intersubband (ISB) transitions in quantum wells prohibit absorption of normally incident light [1]. As a result, light coupling to ISB infrared detectors like quantum well infrared photodetectors (QWIPs) or quantum cascade detectors (QCDs) have been typically accomplished by polishing a 45 degree facet on the detector, or using Brewster's angle geometry - many recent high performance ISB detectors have indeed employed such geometries [2–5]. However, applications in infrared imaging and sensing often require normal light incidence on the detector. Over the past several years, various techniques have been developed to achieve normal-incidence absorption. The most common method is the use of 2-dimensional gratings [6, 7], often employed in focal plane array detectors [8]. A similar idea was to etch gratings directly onto the multiple-quantum well layer to take advantage of near-field coupling [9]. However, the theory of 2-D gratings is highly non-trivial and has been the topic of numerous studies [10, 11]. Moreover, all of the approaches involving gratings are wavelength selective and often require complicated fabrication procedures. Specifically, the spectral shape and peak wavelength are highly dependent on the size and period of the gratings. More recent approaches to achieve normal incidence detection exploits surface plasmons that also act as a waveguide or a plasmonic lens [12–16]. In addition to conventional ISB detectors using conduction band ISB transitions, there were multiple attempts to achieve normal incidence using p-type QWIPs, where band-mixing between the light and heavy hole valence band subbands partially relaxed the ISB polarization selection rule [17, 18]. More recently, nanophotonic techniques like photonic crystal slabs [19], and quantum-dot based devices [20] were used to develop normal-incident detectors. Lastly, there were also studies that exploited total internal reflection in precisely etched surfaces at 54 degrees in a configuration called corrugated QWIPs [21–23].

In this work, we report on a wavelength-independent technique to achieve normal incidence absorption and simultaneously improve detectivity. This method takes advantage of scattering from the sloped sidewalls of wet-etched mesas by increasing the optical absorption area for scattering without increasing the electrical device area. We achieve this by fabricating spirals and hairpin shaped detectors, and compared their responsivity and dark current limited detectivity to that of a standard rectangular mesa of similar electrical area. Using this method, we observe strong normal-incident absorption with a peak responsivity that is up to 2 times larger, and a detectivity that is 2 orders of magnitude more compared to the standard mesa at 45 de-

gree incidence. It should be noted that the results presented here correspond to large-area single pixel detectors in order to directly compare them with similar proof-of-concept detectors in the literature. While it is not possible to directly extrapolate these results to the performance of multi-pixel detectors, similar techniques can be employed to achieve normal incidence absorption in focal plane arrays.

2. Detector design and characterization

Figure 1(a) shows a portion of the conduction band diagram of a conventional vertical transition QCD centered at $6.6 \mu\text{m}$ designed using a one-band conduction band approximation with an energy-dependent effective mass to account for band non-parabolicity [24]. The design is based on three coupled upper detector states with an average transition energy of 188 meV and a 55 \AA thick extraction barrier. The states in the extractor are nominally separated by one longitudinal optical (LO) phonon in energy to facilitate fast carrier relaxation to the next period. 30 periods of the structure, sandwiched between highly doped $\text{In}_{0.53}\text{Ga}_{0.47}\text{As}$ top (400 nm) and bottom (800 nm) contact layers, were grown using lattice matched $\text{In}_{0.53}\text{Ga}_{0.47}\text{As}/\text{In}_{0.52}\text{Al}_{0.48}\text{As}$ materials by molecular beam epitaxy (MBE) on semi-insulating InP substrate (AXT Inc., resistivity $> 0.5 \times 10^7 \Omega\text{cm}$). The contact layers, as well as the main detection well, were Silicon doped to $1 \times 10^{18} \text{ cm}^{-3}$. These wafers were initially processed into standard $310 \mu\text{m} \times 485 \mu\text{m}$ rectangular mesas using conventional lithography and wet-etching techniques.

Spectral photocurrent was measured using a blackbody source at 900°C . The detector is oriented at 45 degrees to the incoming beam. A Germanium neutral density filter (Ge-NDF) was also placed in the beam path to prevent any interband transition. A photocurrent peak at 1578 cm^{-1} ($6.3 \mu\text{m}$) with a spectral width $\Delta E/E$ of 7% was obtained at 86 K, as shown in Fig. 1(b). The narrow peak width is often seen in QCDs, characteristic of the bound-to-bound nature of the transition. A peak responsivity of 8.8 mA/W, not corrected for the Ge-NDF, was obtained. Activation energy, extracted from an Arrhenius plot of the device dark current-voltage characteristics (see inset of Fig. 1(b)), is measured to be 177 meV, corresponding to direct thermal excitation from the lower state to the upper detector state. The device differential resistance decreases from only 10 k Ω at 86 K, to about 50 Ω at 300 K.

3. Normal-incidence detectors—theory and fabrication

In order to achieve normal incidence absorption, we make use of light scattering at the sloped sidewalls of wet-etched mesas. We consider the first two transmissions inside the device as shown in the schematic in Fig. 2(a). The fraction of light transmitted into the device can be calculated by modifying Snell's law for a medium with a continuous range of incident angle. These equations are given by,

$$I_t^{(1)} = \frac{I_o}{\pi} \int_0^{\pi/2} (1 - R_\theta) \left(\frac{\sin \theta}{n} \right)^2 d\theta \quad (1)$$

$$I_t^{(2)} = \frac{I_o}{\pi} \int_0^{\pi/2} R_\theta (1 - R_\theta) \left(\frac{\sin \theta}{n} \right)^2 d\theta \quad (2)$$

where $I_t^{(1)}$ and $I_t^{(2)}$ refer to the first and second light transmission, I_o is the incident light intensity, R_θ is the average reflectivity of the sloped sidewall as a function of the incident angle θ obtained using Fresnel's equations, and the fraction $\left(\frac{\sin \theta}{n} \right)^2$ accounts for the polarization selection rule in the active region. The refractive index of the active region is denoted by n .

The sidewall has been modeled as a quadrant of an ellipse as shown in Fig. 2(b) - this is chosen because the vertical etch-rate of the solution is typically about twice that of the lateral etch-rate. We note that not all incident angles are equally probable - for an elliptical sidewall,

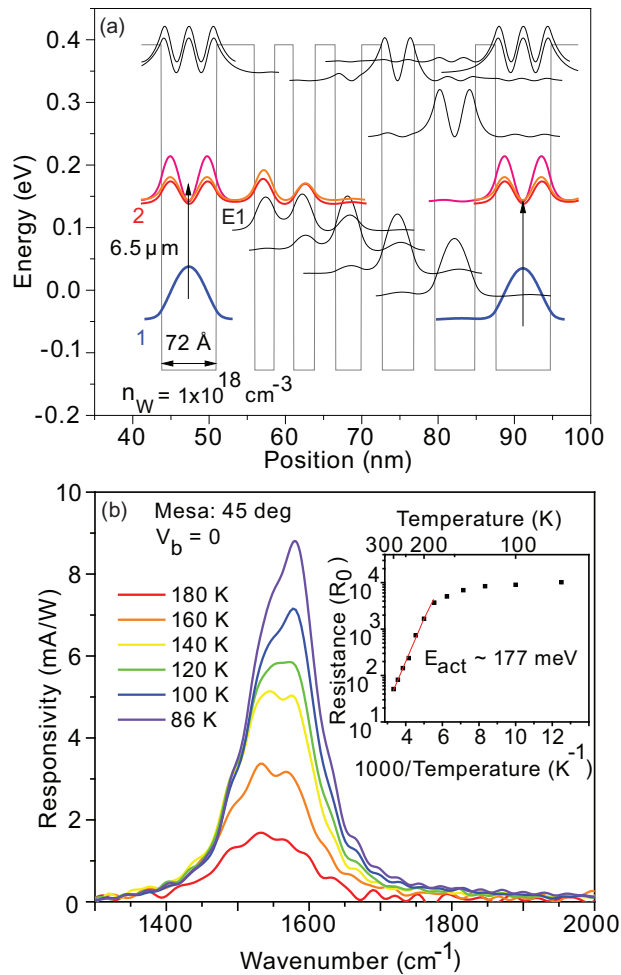


Fig. 1. (a) One period of the conduction band of the detector used in this study. The layer thickness, in Angstroms, from the widest well on the left, are, 72/**50**/26/**25**/28/**27**/34/**27**/41/**27**/52. The In_{0.47}Ga_{0.53}As wells are in regular font, while the In_{0.52}Al_{0.48}As barriers are in bold font, with the underlined layers Silicon doped to $1 \times 10^{18} \text{ cm}^{-3}$. (b) Temperature dependent spectral photocurrent characteristics of the mesa. We obtain a peak wavenumber of 1578 cm^{-1} with a width (in Energy) of only 7% at 80 K. We also obtain a peak responsivity of 8.8 mA/W. (inset) Arrhenius plot of the device differential resistance, showing an expected activation energy of 177 meV.

shallow incident angles (near the bottom of the trench) are more likely for a parallel incident beam. To account for this, we can convert $d\theta$ in Equations 1 and 2 to corresponding values in linear space, dx , that are uniformly spaced using parametric equations. The total absorption efficiency as a function of the trench width, 'a', is shown in Fig. 2(c). Here, we have assumed that the ratio of 'a' to 'b' is 0.5, typical of our etchant solution. For a trench width ranging from $2\ \mu\text{m}$ to $10\ \mu\text{m}$, the total absorption efficiency increases from about 3% to about 12%. In all cases, we also notice that the absorption efficiency is higher than that of the conventional mesa device at 45 degree incidence. At a trench width of $7\ \mu\text{m}$ used in this study, the total absorption efficiency comes to about 8%. Finally, we note that the calculations performed here only corresponds to the geometrical aspect of the detector configuration, and does not take into account variations in the absorption coefficient of the active region or the effect of its location.

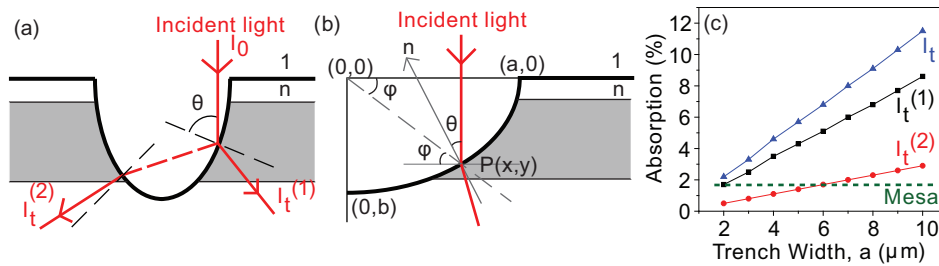


Fig. 2. (a) Schematic ray-diagram representation of light scattering in the wet-etched side-walls of a QCD, with the active region shaded in gray (b) The slope of the sidewalls has been modeled as a quadrant of an ellipse, with a trench width of 'a', and (c) calculated absorption efficiency of the structures as a function of the trench width, with the green dotted line representing the absorption efficiency of a mesa device at 45 degree incidence.

The spiral and hairpin shaped detectors were fabricated using conventional lithography and wet-etching techniques. The designed ridges were $12\ \mu\text{m}$ wide, with a separation of $5\ \mu\text{m}$ between them. The isotropic nature of wet-chemical etching resulted in a ridge of width $9\ \mu\text{m}$, with the separation increasing to $7\ \mu\text{m}$. The inner radius of the innermost spiral, and the length of one arm of the hairpin was $50\ \mu\text{m}$, and $500\ \mu\text{m}$, respectively. The total number of spiral and hairpin arms were designed to keep the electrical area of the device the same as the mesa, about $1.6 \times 10^{-3}\ \text{cm}^2$. The backside surfaces of all devices were mirror polished to avoid spurious reflections from contributing to optical absorption. Optical and SEM images of the fabricated devices can be seen in Fig. 3. The SEM images show a significant 'flat' region at the bottom of the trenches. This region does not contribute to photocurrent due to polarization selection rules, and therefore the absorption efficiency is not affected. However, optimization of the etching process can reduce the footprint of the device, especially in multi-pixel applications. Furthermore, it should be noted that side-wall passivation with appropriate anti-reflection coatings can increase absorption efficiency and reduce generation-recombination related dark current noise.

4. Results and discussion

Dark current characteristics were measured for both the spirals and hairpin-shaped detectors as a function of temperature. Their respective Arrhenius plots, are shown in Fig. 4. In both cases, we can extract an activation energy of about 180 meV, identical to the one obtained from measurements of the mesa device (see Fig. 1). However, we can notice a significant difference in the absolute values of the differential resistance at zero bias. For the spirals, R_0 varies from a high of about $66\ \text{M}\Omega$ at 80 K to about $150\ \Omega$ at 300 K, while for the hairpin detectors, this value ranges from about $17\ \text{M}\Omega$ to $110\ \Omega$. In comparison, the R_0 values for the mesa device was

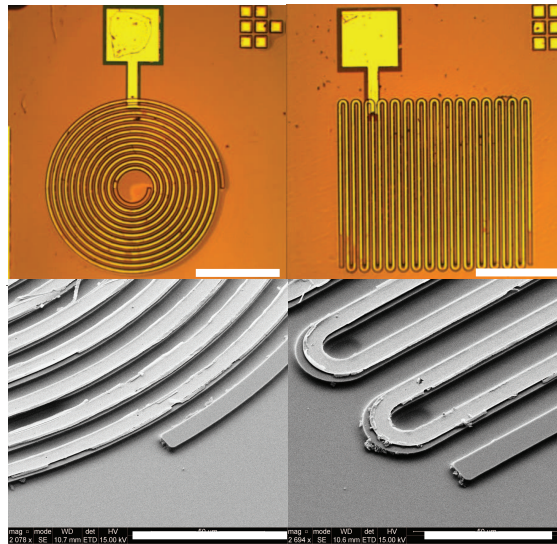


Fig. 3. Optical and Scanning Electron Microscope (SEM) images of the fabricated spirals and hairpin detectors. Moving clockwise from the top left, the scale bars represent dimensions of $200\ \mu\text{m}$, $200\ \mu\text{m}$, $50\ \mu\text{m}$, and $50\ \mu\text{m}$, respectively. The total electrical area of the spirals and waves are very similar to that of the mesa device, about $1.6 \times 10^{-3}\ \text{cm}^2$.

only $10\ \text{k}\Omega$ at $80\ \text{K}$, decreasing to $50\ \Omega$ at $300\ \text{K}$. This three orders of magnitude larger differential resistance at lower temperatures for spirals and waves compared to the mesa device arises because of the interplay between in-plane (R_{\parallel}) and out-of-plane resistance (R_{\perp}). At low temperatures, the spiral and hairpin detectors have high R_{\parallel} and R_{\perp} , resulting in a high differential resistance. For a bulk mesa device, the in-plane resistance (R_{\parallel}) is low even at low temperatures - in the case of spirals/hairpins, this in-plane conduction has been severely restricted because of the geometry of the device, resulting in a larger R_0 . Conversely, at high temperatures, the out-of-plane resistance ($R_{\perp} \approx 50\ \Omega$) approaches that of the in-plane resistance (typically about a few ohms to tens of ohms) and the difference between mesa and the spirals/hairpins is not as significant.

The temperature-dependent *normal-incident* spectral photocurrent characteristics of both the spirals and hairpins can be found in Fig. 5, taken using an FTIR broadband source chopped at $279\ \text{Hz}$ and measured with standard lock-in techniques. In both geometries, we obtain a peak photocurrent at $1528\ \text{cm}^{-1}$ ($6.5\ \mu\text{m}$), and a full-width at half maximum (FWHM) of $107\ \text{cm}^{-1}$ ($\Delta E/E \approx 7\%$) for the spirals and $110\ \text{cm}^{-1}$ ($\Delta E/E \approx 7.2\%$) for the hairpin detectors. These values are almost identical to those measured with standard mesa devices (see Fig. 1). Because the peak wavelength and width in the spiral and hairpin detector configurations did not change compared to conventional mesa devices, the spectral response of these new geometries are wavelength independent. However, the differences in responsivity between the spirals and the hairpin shaped detectors can arise because of two factors - (i) the actual slope of the side-wall is different for spirals and hairpins due to geometry and the properties of the etchant solution, resulting in slight variations in optical absorption, and (ii) the impedance of the two structures under illumination are different, resulting in differences in observed photocurrent.

The responsivity values given here corresponds to those taken with the Ge-NDF in the beam path of the blackbody source. It should be noted that the transmission of the neutral density filter is about 30% indicating that true responsivity values without the filter can be up to 3 times larger. As mentioned previously, the Ge-NDF filter is used to prevent interband transitions from

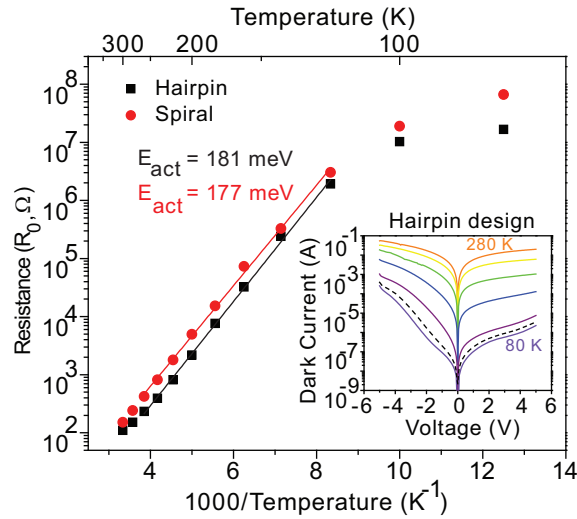


Fig. 4. Arrhenius plots of the device differential resistance of the spirals (red circles) and hairpins (black squares) at zero bias. In both cases, we extract an activation energy of about 178 meV. Compared to standard mesa devices, we obtain 3 orders of magnitude larger device differential resistance at low temperatures because of the increased in-plane resistance. The inset shows the temperature dependent device I-V characteristics of the hairpin detector; the dotted line represents the 300 K background photocurrent measured at a device temperature of 80 K.

contributing to the measured photocurrent. We obtain peak responsivities of 6 mA/W and 12.3 mA/W for the spirals and hairpins, respectively. Using this value of measured responsivity and the estimated absorption efficiency, one can estimate the quantum efficiency of these detectors using the relation, $R_p = \frac{\lambda_p}{hc} \eta g$, where R_p is the peak responsivity at wavelength λ_p , η is the absorption efficiency, and g is the photoconductive gain. The estimated quantum efficiency of the device is approximately 2%, typical of ISB detectors. While reducing the number of periods will increase the efficiency, it will also reduce the absorption efficiency.

Figure 6 shows the temperature dependence of dark current limited detectivity (D_j^*) of the spirals and hairpins at normal-incidence absorption, in comparison to mesa detectors at 45 degree incidence. We obtain peak detectivities of $2.8 \times 10^{10} \text{ cm}\sqrt{\text{Hz}}/\text{W}$ for the spirals, $2.9 \times 10^{10} \text{ cm}\sqrt{\text{Hz}}/\text{W}$ for the hairpins, and $2.9 \times 10^8 \text{ cm}\sqrt{\text{Hz}}/\text{W}$ for the mesa detectors, at 80 K. The combination of a higher differential resistance and increased optical coupling has resulted in a 2 orders of magnitude improvement in the detectivity of the spirals and hairpins. This large difference reduces with increasing temperature, resulting in peak D_j^* of $1.7 \times 10^7 \text{ cm}\sqrt{\text{Hz}}/\text{W}$ for the hairpins, $1.4 \times 10^7 \text{ cm}\sqrt{\text{Hz}}/\text{W}$ for the spirals, and $8.4 \times 10^6 \text{ cm}\sqrt{\text{Hz}}/\text{W}$ for the mesa detectors at a temperature of 200 K. This is because the role of a large in-plane resistance of spirals and wavy resulting in higher R_0 diminishes with increasing temperature. Nevertheless, the spirals and hairpins far outperform mesa devices at lower temperatures, and absorb normally incident light.

5. Conclusion

In summary, we have developed a novel technique for normal incidence absorption in ISB detectors by taking advantage of light scattering along sloped sidewalls of wet-etched mesas. We fabricated detectors in the shape of spirals and hairpins, and compared them to a standard rectangular mesa of similar device electrical areas. We obtain a peak responsivity of about 6 mA/W

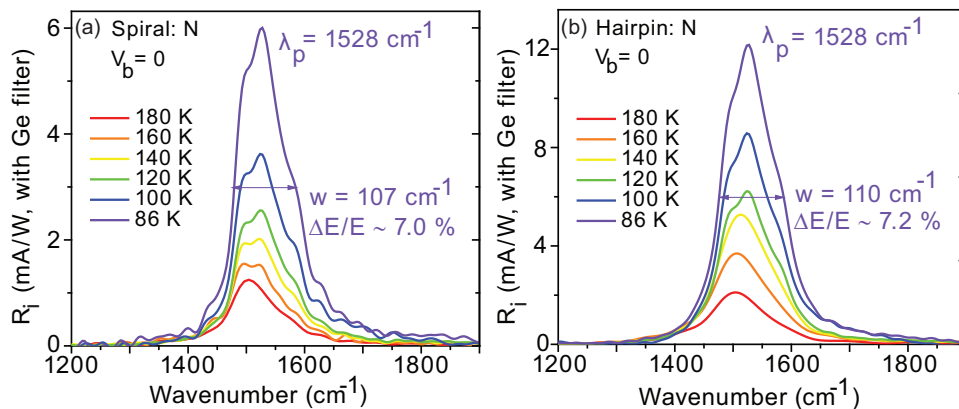


Fig. 5. Normal incident spectral photocurrent measurements of (a) spiral detectors, and (b) hairpin detectors, taken from 80 K to 180 K. In both cases, we see peak emission at 1528 cm^{-1} and a FWHM of about 110 cm^{-1} , corresponding to a narrow width of only about 7%. This width matches the one measured with the mesa devices. The figure also shows two values of responsivity for the detectors - the left axis corresponds to a responsivity measured with a Ge-NDF, while the right axis corresponds to responsivity without the filter.

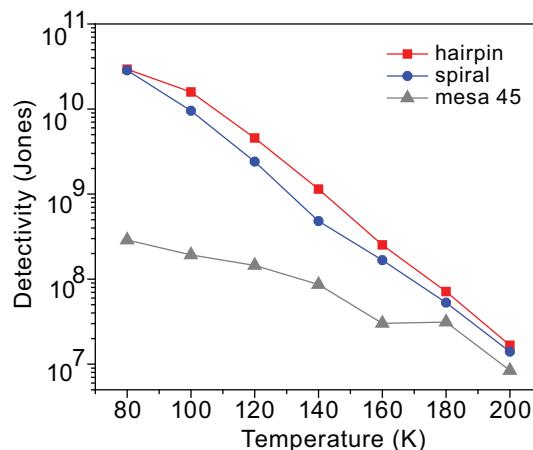


Fig. 6. Johnson noise limited detectivity (D_j^*) of the hairpin (red squares), spiral (blue circles), and mesa (gray triangles) detectors as a function of temperature. These values are calculated using the responsivity taken with the Ge filter, and therefore represent a lower bound on D_j^* .

for the spiral and 12 mA/W for the hairpin detectors at normal incidence, comparable to the 8.8 mA/W obtained for the mesa at 45° incidence. In addition, we also obtain a 2 orders of magnitude increase in the background limited detectivity at 80 K. This method to achieve normal incidence absorption is wavelength independent, and does not involve complicated fabrication procedures, paving the way for more widespread use of ISB detectors. Although the device performance presented here are superior to standard mesa devices, further work is needed to study the effect of such novel structures in multi-pixel configuration.

Funding

National Science Foundation (NSF) MIRTHE (EEC-0540832) award.